

Bessel-modulated autofocusing beams for optimal trapping implementationFuxi Lu,^{1,*} Hao Wu,^{2,*} Yi Liang^{①,1,3,†} Liu Tan,¹ Zhifu Tan,¹ Xu Feng,¹ Yi Hu,^{2,‡} Yinxiao Xiang,³ Xubo Hu,^{3,4} Zhigang Chen^{②,2,3,§} and Jingjun Xu^②¹*Guangxi Key Lab for Relativistic Astrophysics, Center on Nanoenergy Research, School of Physical Science and Technology, Guangxi University, Nanning, Guangxi 530004, China*²*The MOE Key Laboratory of Weak-Light Nonlinear Photonics, TEDA Applied Physics Institute and School of Physics, Nankai University, Tianjin 300457, China*³*Department of Physics and Astronomy, San Francisco State University, San Francisco, California 94132, USA*⁴*College of Electronic Engineering, South China Agricultural University, Guangzhou 510642, China*

(Received 16 April 2021; accepted 7 October 2021; published 25 October 2021)

Abruptly autofocusing beams were proposed and tested for a variety of applications such as optical manipulation, yet their trapping performance associated with the optical forces and trap stiffness remains largely unexplored. In this work, we design and demonstrate specially modulated autofocusing beams. We theoretically and experimentally show improved properties of such beams and their trapping capabilities as compared to their unmodulated counterparts. In particular, an autofocusing beam tailored with a Bessel function exhibits a shorter focal length and a much stronger peak intensity than that of an unmodulated circular Airy beam. Moreover, we perform optical tweezer experiments using both the modulated and unmodulated autofocusing beams to trap microbeads and red blood cells for direct comparison, and find that the Bessel-modulated beam displays an enhanced trapping capability, thanks to a stronger optical trapping force due to its peculiar intensity landscape. Compared with the conventional circular Airy beams, optical tweezers based on our modulated autofocusing beams exhibit a superior performance, which may lead to new photonic tools for optical trapping and manipulation.

DOI: [10.1103/PhysRevA.104.043524](https://doi.org/10.1103/PhysRevA.104.043524)**I. INTRODUCTION**

In the past five decades, optical tweezers have attracted a great deal of attention, leading to numerous applications demonstrated in a variety of fields including optics and photonics, biophotonics and cell biology, colloid and aerosol sciences, and statistical physics [1–5]. Conventional optical tweezers, commonly based on Gaussian beams, are often afflicted with some invasive effects like photodamage or heating of biological samples, partially arising from prolonged light exposure or high trapping power [3,4,6,7]. To reduce these adverse influences, many efforts have been taken for improving the tweezing techniques. Indirectly, the photodamage was reduced via tethering biological samples to attached beads [4,6]. More directly, structured light is employed aiming for this improvement. For instance, the so-called “dark beams,” represented by the higher-order Gaussian-Laguerre doughnut-shaped beams and optical vortex beams [8], were utilized to achieve a low photodamage. Along this line, various optical tweezers techniques based on novel optical fields have been developed, driven by the dynamically changing field of beam shaping and structured light [9].

About a decade ago, the so-called “abruptly autofocusing beams” originated from self-accelerating radially symmetric *circular Airy beams* (CABs) [10–25] brought about new tools for shaping the optical tweezers. Compared with Gaussian beams which build up the peak intensity gradually during evolution, these intriguing CABs exhibit an abruptly focusing behavior that leads to a huge intensity gradient in both longitudinal and transversal directions. Due to the quite short distance of power accumulation, both photodamage and heating can be somewhat reduced or more localized. Triggered by this exotic feature, the autofocusing beams have been widely touted and tested for applications in optical manipulations and tweezers techniques [12,21–23]. However, to the best of our knowledge, quantitative characterization of their trapping forces and further optimizing their performance remain largely unexplored, especially in the domain of experimental studies [21–23].

In this work, we propose and demonstrate a class of *modulated autofocusing beams* (MABs), and directly compare them with conventional circular autofocusing beams in the aspects of trapping forces and stiffness both theoretically and experimentally. We find that an MAB exhibits a sharper contrast, a higher peak intensity, and a shorter autofocusing distance as compared to a CAB. Based on the wave theory analysis [26–28], these improved features are well explained by the two components of the MAB. In the experiments with trapping microparticles and red blood cells (RBCs), the MAB always shows a larger trapping stiffness (thus accordingly a

*These authors contributed equally to this work.

†liangyi@gxu.edu.cn

‡yihu@nankai.edu.cn

§zgchen@nankai.edu.cn

stronger trapping force) than that of the CAB. Our results may bring about new possibilities for developing optical manipulation tools based on such unconventional optical beams for biomedical applications.

II. THEORY AND ANALYSIS

Generally, a traditional autofocusing CAB is designed via a radially symmetric Airy beam with inward acceleration. At the input, its intensity profile consists of many concentric rings with the most intense one being inside. Theoretically, the input amplitude is formulated as $\text{Ai}(r_0 - r) \exp[a(r_0 - r)]$, where $\text{Ai}(\cdot)$ represents the Airy function, r_0 is an initial radial position of most intense ring, and a is an apodization factor determined by the effective aperture of an optical system, $r = \sqrt{x^2 + y^2}$ is the radial coordinate, and x and y are the transversal coordinates [10]. To enhance the peak intensity, we impose an additional Bessel modulation on the CAB (see details in the Appendix). Specifically, the electric field of the modified CAB (or MAB) is prescribed as

$$\psi(r, z = 0) = A_0 \text{Ai}\left(\frac{r_0 - r}{w}\right) \exp\left(\alpha \frac{r_0 - r}{w}\right) \times \exp\left(iv \frac{r_0 - r}{w}\right) J_0\left(\frac{r_1 - r}{w}\right), \quad (1)$$

where J_0 represents the Bessel function, w is a radial scale factor determining the width of the most intense ring, and $v = \theta kw$ is a radially kicked velocity associated with the initial launching angle θ of this beam, and r_1 is a parameter to control the modulation of the Bessel function.

To investigate the propagation properties of this modified autofocusing beam in simulation, we use the field in Eq. (1) as the input of the paraxial diffraction equation [29,30]:

$$\partial_{xx}^2 \psi + \partial_{yy}^2 \psi + 2ik \partial_z \psi = 0, \quad (2)$$

where Ψ is the complex amplitude of an electric field, $k = 2\pi n/\lambda$ is the wave number, n is the refractive index, λ is the wavelength of the incident light, and z is the propagation distance.

For a better comparison, a CAB and its modified version are designed for reaching the maximum peak intensity at the same distance (where a focal point is defined). In doing so, the following parameters are adopted as an example: $r_0 = 120 \mu\text{m}$, $a = 0.13$, and $v = -2$, $\lambda = 960 \text{ nm}$, $w = 24 \mu\text{m}$, $r_1 = 300 \mu\text{m}$ for an MAB, while $w = 20.3 \mu\text{m}$ and $r_1 = r$ for a CAB. The incident light powers are the same

(here 1 W) for both cases. Figure 1 shows the numerical propagation results of the two beams. Kicked with the initial launching velocity, the rings of CAB expand then shrink and finally abruptly focus at a certain position [Figs. 1(a1)–(a3)]. As usual, the peak intensity is always located in the inner ring. Once introducing the modification, the resulting MAB exhibits a similar autofocusing propagation process, but differently, its peak intensity shifts from the inner ring towards outside during propagation accompanying with a narrowing ring width [Figs. 1(b1)–1(b3) and 1(d)]. Such a feature leads to a much higher peak intensity and stronger intensity contrast at the focal point for MAB as shown in Figs. 1(c) and 1(e), respectively. These distinctive results can be well interpreted via analyzing the internal transverse power flow. Figures 1(a3) and 1(b3) present the scenarios at the focal point for both beams. Clearly, the inward power flow of MAB is stronger and more concentrated comparing to CAB, thereby causing a larger peak intensity.

We further examine how the autofocusing property of MAB changes with the value of r_1 in the Bessel modulation. As shown in Fig. 2(a), for most cases, MAB shows a stronger peak intensity than CAB. In particular, almost one order of magnitude enhancement can be reached at around $r_1 = 500 \mu\text{m}$ [Fig. 2(a)]. One should avoid the range of $0 < r_1 < 240 \mu\text{m}$, where MAB exhibits otherwise a lower peak intensity. For different values of r_1 , the autofocusing length keeps nearly constant [inset in Fig. 2(a)].

To further understand how the Bessel function modulates the property of MAB, an asymptotical wave analysis in the framework of the geometrical optics is applied [26–28]. Based on the asymptotic expression of the Bessel function, i.e., $J_0(x) \approx (2/\pi x)^{1/2} \cos(x - \pi/4)$, Eq. (1) can be simplified as

$$\psi(r, z = 0) \approx A_0 \sqrt{\frac{w}{2\pi(r_1 - r)}} \exp\left(\alpha \frac{r_0 - r}{w}\right) [\psi_+(r, z = 0) + \psi_-(r, z = 0)], \quad (3)$$

where $\psi_{\pm}(r, z = 0) = \text{Ai}\left(\frac{r_0 - r}{w}\right) \exp\{i[(v \pm 1)\frac{r_0 - r}{w} \pm \frac{r_1 - r_0}{w} \mp \frac{\pi}{4}]\}$. Compared with a radially kicked CAB formulated as $\text{Ai}\left(\frac{r_0 - r}{w}\right) \exp(iv \frac{r_0 - r}{w})$, one can infer from Eq. (3) that MAB indeed consists of two CABs with different kicked velocities. The components with the velocity $v + 1$ and $v - 1$ are denoted as CAB_+ and CAB_- , respectively. Their interference leads to an oscillatory dependence for the peak intensity of MAB to the parameter r_1 . In order to obtain the exact trajectory of MAB, the caustics are calculated with the help of ray analysis. Via the geometrical optics method, Eq. (3) is further transformed as

$$\begin{aligned} \psi(r, z = 0) &= E_0^+ \exp(i\varphi_0^+) + E_0^- \exp(i\varphi_0^-), \\ \varphi_0^{\pm} &= v \frac{r_0 - r}{w} + \arcsin \left\{ \frac{\cos\left[\frac{2}{3}\left(-\frac{r_0 - r}{w}\right)^{3/2} - \frac{r_1 - r}{w}\right] \pm \sin\left[\frac{2}{3}\left(-\frac{r_0 - r}{w}\right)^{3/2} + \frac{r_1 - r}{w}\right]}{2\left[1 \pm \sin\left(2\frac{r_1 - r}{w}\right)\right]} \right\}, \\ E_0^{\pm} &= \left[\mp i \pm i \sin\left(2\frac{r_1 - r}{w}\right) \right] A_0 \sqrt{\frac{w}{2\pi(r_1 - r)}} \exp\left(\alpha \frac{r_0 - r}{w}\right) \left(-\pi^2 \frac{r_0 - r}{w}\right)^{-1/4}. \end{aligned} \quad (4)$$

To obtain the above formula, $\text{Ai}(x) \approx (-\pi^2 x)^{-1/4} \sin\left[\frac{2}{3}(-x)^{3/2} + \frac{\pi}{4}\right]$ ($x < 0$) is employed. Then, we can

calculate the corresponding radiation rays whose caustics are described by $R = r + z \tan[\sin^{-1}(\partial_r \varphi_0^{\pm})]$, as seen

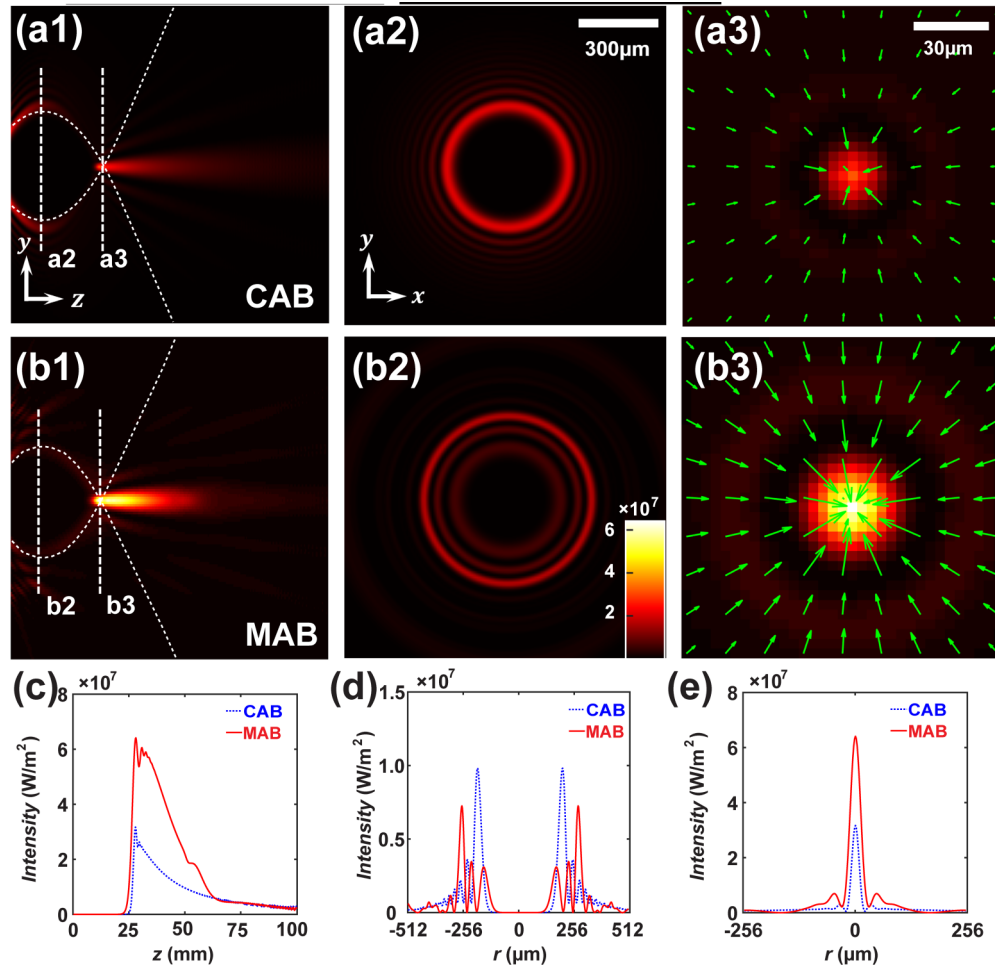


FIG. 1. Numerical simulations. Direct comparison of propagation dynamics between (a) a CAB and (b) an MAB. (a1), (b1) are side views of 100-mm-long beam propagation. (a2), (a3) and (b2), (b3) are plots of corresponding beam profiles at locations marked by the dashed vertical lines in (a1) and (b1), respectively. (a3) and (b3) also present the transverse power flow. (c) Peak intensity of CAB and MAB along propagation; (d), (e) radial intensity distribution corresponding to (a2), (b2) and (a3), (b3), respectively. White dotted curves in (a1) and (b1) indicate the trajectories of the innermost ring of the beams. Intensities in (a2) and (b2) are enlarged about 2 times for better visualization.

in Fig. 2(b). From these rays, we can get the exact trajectory of MAB [marked by red line in Fig. 2(b)]. Also, Fig. 2(b) presents the trajectory of CAB calculated by $r_{\text{CAB}} = r_0 + v_z/kw - z^2/4k^2w^3$ [14] with the parameters adopted in Fig. 1 (r_{CAB} indicates the radial position of the innermost ring of CAB in propagation, marked by a blue circle line). Clearly, these two trajectories are very close and consistent with the simulating results in Fig. 1 [marked by the white dotted line in Figs. 1(a1) and (b1)]. Furthermore, from the trajectories of MAB and its components in Fig. 2(c), one can see that the focusing points of CAB₊ and MAB almost overlap, appearing much earlier than that of CAB₋ during evolution. Without the Bessel modulation, MAB reduces to CAB that always shows a longer focal length in the absence of the faster autofocusing component (see the CAB case that has the same parameter as MAB $w = 24 \mu\text{m}$ in the Appendix). That is the reason why we should reduce the parameter w to reach an identical focal position for the modulated and unmodulated cases. In Eq. (3), since the parameter r_1 merely introduces constant amplitude and phase changes for the whole beam profile, it can hardly

alter the autofocusing dynamics and thus almost exerts no influence on the autofocusing length. Using Eq. (3), the peak intensity and the focusing length are recalculated, showing a good agreement with the ideal case [Fig. 2(a)], validating our theoretical approximation.

Next, we investigate the optical tweezer capabilities of these autofocusing beams by characterizing their trapping forces. Theoretically, in the framework of dipole approximation, their trapping forces F_{trap} including the gradient force F_g and the scattering force F_s on a Rayleigh particle are calculated via the following formulas [5,21–23]:

$$\begin{aligned} F_g &= \frac{1}{4} \varepsilon_0 \varepsilon_m \text{Re}(\alpha) \nabla |\psi^2|, \\ F_s &= \frac{1}{12\pi} \varepsilon_0 \varepsilon_m^3 k^4 |\alpha|^2 |\psi^2|, \end{aligned} \quad (5)$$

where ε_0 is the dielectric constant in vacuum, $\alpha = 4\pi R^3(\varepsilon_p - \varepsilon_m)/(\varepsilon_p + 2\varepsilon_m)$ is the polarizability, R is the radius of the particle, and ε_p and ε_m are dielectric functions of the particle and the surrounding medium, respectively.

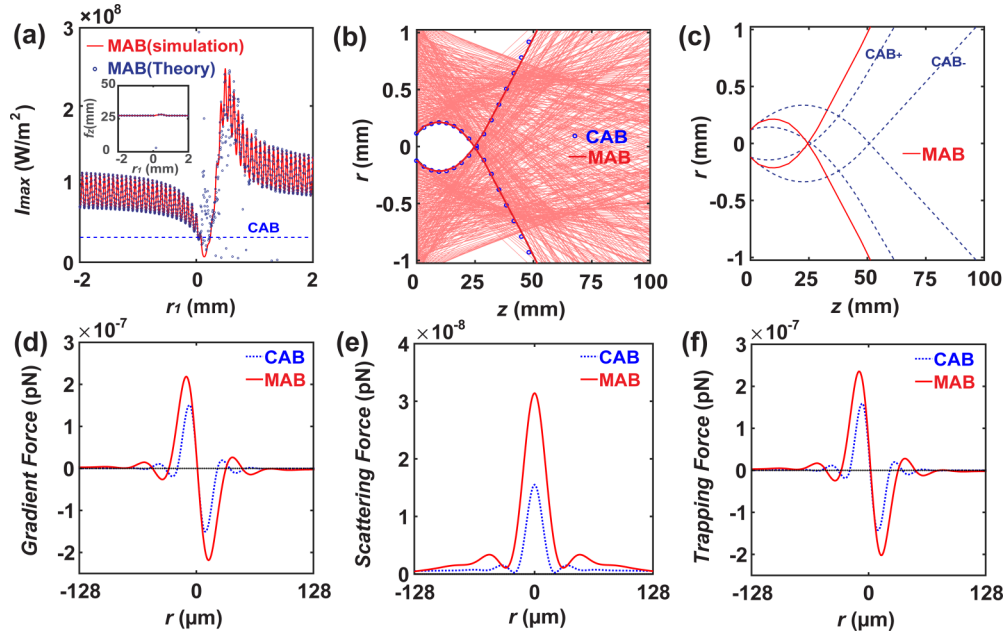


FIG. 2. (a) Peak intensity at the focal point and autofocusing length f_z (inset) with different r_1 for MAB [red curve from simulation and black-blue circle calculated from Eq. (3)] and for CAB (blue dotted line). (b) Ray description (thin red line) of MAB overlapping with thick red line and blue dotted circles indicating the trajectories of CAB and MAB in Fig. 1, respectively. (c) Trajectories of MAB and its two components. (d) The transversal gradient forces, (e) transversal scattering forces, and (f) total trapping forces of CAB and MAB at the focusing point.

Figures 2(d)–2(f) show the calculated gradient force, scattering force, and the total trapping force along the same

direction ($F_{\text{trap}} = F_g + F_s$) for CAB and MAB to trap a polystyrene bead (diameter is 40 nm) in water ($\epsilon_p = 2.5$,

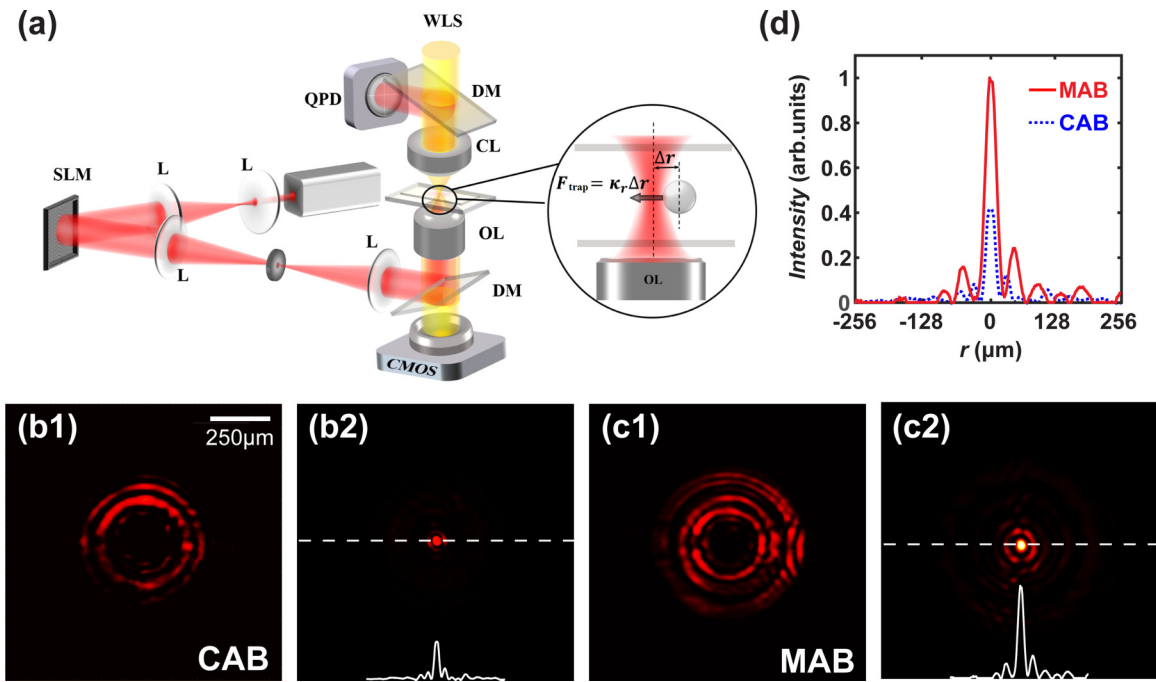


FIG. 3. (a) Experimental setup for optical tweezers based on autofocusing beams. L: lens, SLM: spatial light modulator, DM: dichroic mirror, OL: high NA objective lens, CL: condenser lens, WLS: white light source, CCD: camera, QPD: quadrant photodiode. The inset illustrates a trapped bead under the action of the tweezers. (b), (c) experimentally obtained transverse profiles of (b) a CAB and (c) an MAB at two chosen propagation distances. Intensities in (b1) and (c1) are enlarged about 3 times for better visualization and comparison. (d) Beam profiles of CAB and MAB along the dashed lines in (b2) and (c2). Note that the measurement is performed before the beam enters the objective lens.

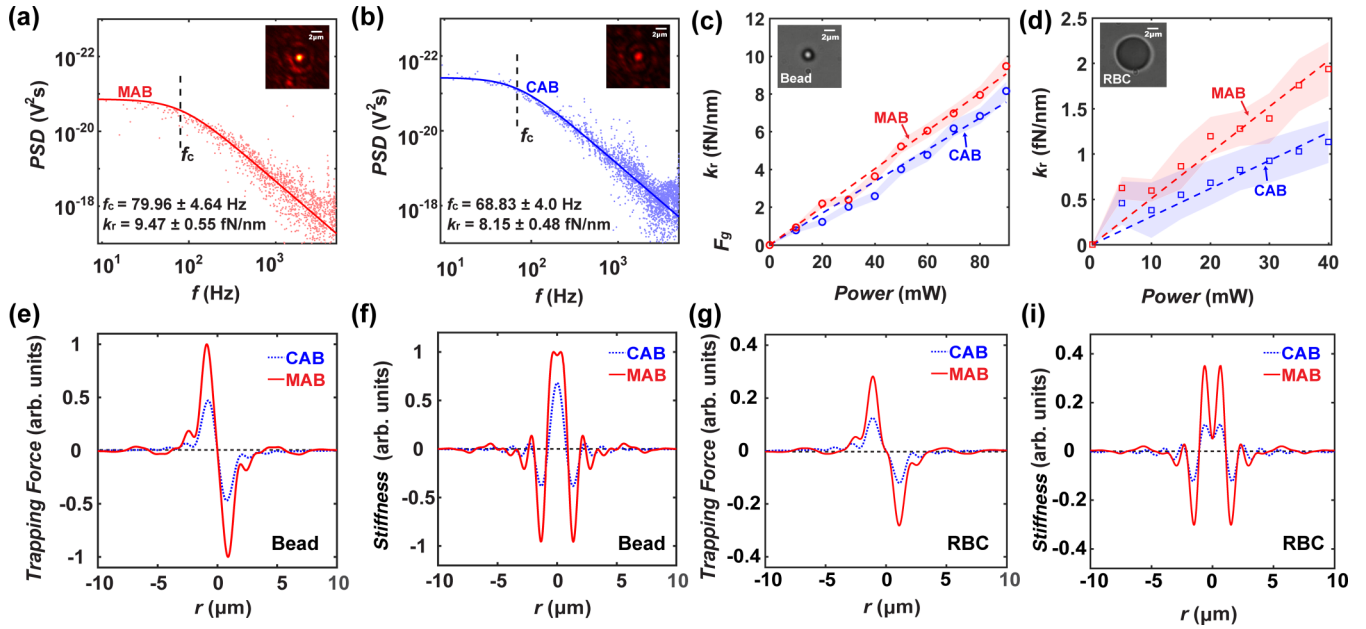


FIG. 4. (a), (b) Measured power spectra from the optical tweezers showing the trap stiffnesses κ_r of a $2\text{-}\mu\text{m}$ polystyrene bead for (a) MAB and (b) a CAB that are presented in the insets. Solid lines describe their relative power spectrum fitting and black dashed lines mark the positions of the corner frequency. (c), (d) Trapping stiffnesses κ_r for two different beams as a function of input power exerting on (c) a $2\text{-}\mu\text{m}$ polystyrene bead and (d) an $\sim 5\text{-}\mu\text{m}$ RBC. The uncertainties are indicated by the shaded regions. (e)–(i) Calculated transverse trapping force and trap stiffness of the CAB and the MAB based on the full-wave generalized Lorenz-Mie theory and Maxwell stress tensor technique [31] for (e), (f) a polystyrene bead and (g), (h) an RBC. Note that the values in (g) and (h) are normalized by using the maximum values associated with the MAB in (e) and (f), respectively.

$\epsilon_m = 1.7$). We can see that the MAB seems to exhibit a larger trapping force than the CAB does, as further analyzed below using the full-wave generalized Lorenz-Mie theory [31].

III. EXPERIMENTS AND DISCUSSION

In order to verify the above analysis, we performed a series of experiments to investigate propagation dynamics and optical trapping capabilities of CABs and MABs. The experimental setup is similar to the one used in our previous work [19]: a linearly polarized Gaussian beam with a wavelength of $\lambda = 960\text{ nm}$ is launched onto a spatial light modulator (SLM) with the predesigned phase modulations, and in the following, a Fourier lens is used to turn the Gaussian beam into a CAB or MAB. The imposed phases are obtained by calculating the Fourier transform hologram of each beam. Then a charge-coupled device (CCD) camera is employed to monitor their intensity patterns. The measured profiles of CAB and MAB are presented in Figs. 3(b) and 3(c), respectively. Similar features are observed as in our simulation: The main ring of MAB is narrower than that of CAB; The peak intensity in MAB is larger than that of CAB at focal point [Fig. 3(d)].

To study the trapping capability of the beams in optical tweezers, we add one more lens in the propagation path to form a $4f$ system, delivering the Fourier distributions of CAB and MAB to the front of an objective (oil immersion) placed in a typical microscopic system, as shown in Fig. 3(a). Under proper conditions, the trapping potential is approximately treated as in the scenario described by a spring [as

schematically shown in the inset of Fig. 3(a)]. The spring stiffness is proportional to the trapping force, thereby enabling the characterization of the trapping capability. Based on the Langevin equation, one can get the trapping stiffnesses of the beams via power spectrum analysis method [1–4,32]. In this approach, the trapped particle positions in the trapping are firstly measured by a quadrant photodiode that collects (assisted with a condensed lens) the scattering light from the particle or cells, and then their power spectra are obtained using the Fourier transform for further calculating the trapping stiffness κ_r ($\kappa_r = -dF_{\text{trap}}/dr$), by also employing the corner frequency power spectrum $f_{c,r}$: $f_{c,r} = \kappa_r/2\pi\gamma$, where $\gamma = 6\pi\eta R$ is the particle friction coefficient, η is the viscosity of the solution, and R is the radius of the trapping object.

Figures 4(a) and 4(b) present the power spectra of CAB and MAB tweezers with a 90-mW input power targeting for a $2\text{-}\mu\text{m}$ polystyrene bead as a test object in water. The beam parameters are adopted following the simulation in Fig. 1. In comparison of the two tweezers, clearly, MAB shows a larger corner frequency, thus leading to an enhanced trapping stiffness and accordingly a stronger trapping force. Since the polystyrene bead has a larger scale compared with the light wavelength, the theoretical model in the framework of dipole approximation [i.e., Eq. (5)] is not quite applicable to our experimental conditions. For such a regime of the Mie scattering, one can use a modified version of Eq. (5) based on multipoles up to the electric octupole or to any order [33,34], or the method based on the full-wave generalized Lorenz-Mie theory and Maxwell stress tensor technique [31]. Here, we employ the latter model to calculate the trapping

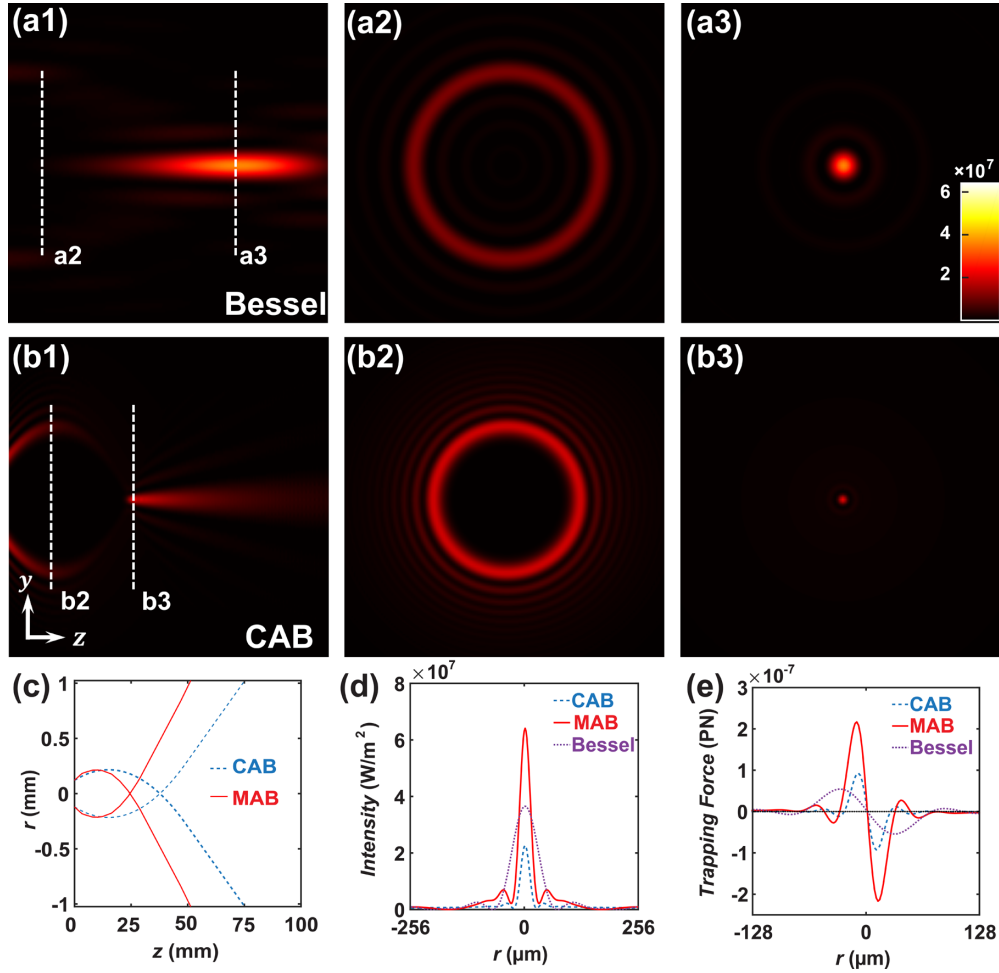


FIG. 5. (a), (b) Direct comparison of the propagation dynamics of (a) Bessel beams [$\psi(r, z=0) = A_0 J_0(\frac{r_1-r}{w})$, $r_1 = 300 \mu\text{m}$] and (b) CAB ($r_0 = 120 \mu\text{m}$, $\alpha = 0.13$, and $v = -2$, $r_1 = r$) with same incident conditions as MAB (1W, $w = 24 \mu\text{m}$, $\lambda = 960 \text{nm}$), respectively. (a1) and (b1) are the 100-mm side-view propagation of the beams. (a2), (b2) and (a3), (b3) plot corresponding beam profiles at locations marked by the dashed vertical lines in (a1) and (b1), respectively. (c) Trajectories of CAB and MAB with same radial scale factor, i.e., $w = 24 \mu\text{m}$. (d), (e) radial intensity distribution and radial gradient forces of Bessel beam, CAB and MAB at the focusing point. Intensities in (a2) and (b2) are enlarged about 2 times for better visualization.

forces for MAB and CAB and further analyze their stiffness. Note that the calculated trapping forces here are composed of the gradient and scattering forces, which can be decomposed using the fast Fourier transform approach [33,35] or the Cartesian multipole expansion theory [34,36]. Since the concerned Mie particles experience a force that is mainly the sum of the gradient force and the scattering force in our experiment, we did not decompose the two components in our analysis.

As shown in Figs. 4(e) and 4(f), for the same size of the bead, an enhancement ($\sim 45\%$) of the stiffness for MAB is approached, which indicates that the difference obtained experimentally for the trapping abilities of the two optical fields is reasonable. But, the stiffness difference measured in experiment is not as sharp as the theoretical prediction. This may attribute to the imperfect experimental conditions. For example, the SLM with a limited resolution is less efficient for generating MAB that is associated with a more complex phase modulation as compared with the case of CAB. The enhancement of trapping stiffness for MAB is further veri-

fied by injecting different input powers. In the chosen power range, the trapping stiffnesses of both tweezers are nearly proportional to the power. In another experiment, an RBC (about $5 \mu\text{m}$) in hypotonic buffer (i.e., with a spherical shape) [32,37] is employed, and two more features are observed: firstly, the stiffness in the MAB tweezers exhibits a relatively larger increase than that in the CAB tweezers [Fig. 4(d)]; secondly, the stiffness for each beam is smaller than that for the same beam to trap the polystyrene bead, which is consistent with the fact that the stiffness is inversely proportional to the size of a trapped particle [1]. These observations are in agreement with our simulations based on the full-wave generalized Lorenz-Mie theory and Maxwell stress tensor technique [Figs. 4(g)–4(i)].

Before conclusion, we should note that the trapping performance of MAB can be further enhanced by choosing proper parameters of the imposed Bessel modulation, as found in our preliminary numerical simulations. These results and corresponding experimental studies will be reported elsewhere.

IV. CONCLUSION

In summary, we have proposed and demonstrated a scheme to modulate and optimize the autofocusing beams for the enhancement of optical trapping capabilities. Through a Bessel modulation, the autofocusing beams are endowed with a stronger peak intensity and a shorter autofocusing length as compared with their unmodulated counterparts. Accordingly, the modulated beams exhibit a larger trapping stiffness (i.e., a stronger trapping force), which is well verified in our optical tweezers experiments with both dielectric particles and RBCs. Our results provide a comprehensive understanding of the optical trapping capabilities of the modulated autofocusing beams, which may find unique applications for optical manipulation and biomedical research, bearing in mind that the autofocusing beams can circumvent obstacles.

ACKNOWLEDGMENTS

This work was supported by the National Natural Science Foundation of China (Grant No. 11604058, 91750204), the National Key R&D Program of China under

Grant No. 2017YFA0303800, the Guangxi Natural Science Foundation (Grants No. 2020GXNSFAA297041, No. 2020GXNSFDA238004, and No. 2016GXNSFBA380244), and the Natural Science Foundation of Guangdong Province (Grant No. 2018A0303130232).

The authors declare no conflicts of interest.

APPENDIX: COMPARISON OF BESSEL BEAM, CAB WITH $w = 24 \mu\text{m}$ AND MAB

As shown in Fig. 5(a), a Bessel beam defined by $J_0(r_1 - r)$ can focus itself to enhance its peak intensity. However, at focal point, its peak intensity is smaller than that of MAB. In addition, Fig. 5(b) shows the propagation of CAB with same parameters as MAB except $r_1 = r$. Compared with MAB, this CAB focuses itself more slowly [Fig. 5(c)]. With the help of the Bessel function, MAB is able to abruptly autofocus in a shorter propagation length and can have more than two times stronger peak intensity at focal point [Fig. 5(d)]. Moreover, MAB shows a largest trapping force among the three cases, implying a better performance in optical tweezer [Fig. 5(f)].

-
- [1] P. Jones, O. Maragò, G. Volpe, P. Jones, O. Marago, and G. Volpe, *Optical Tweezers: Principles and Applications* (Cambridge University Press, Cambridge, 2015).
 - [2] D. Gao, W. Ding, M. Nieto-Vesperinas, X. Ding, M. Rahman, T. Zhang, C. Lim, and C.-W. Qiu, Optical manipulation from the microscale to the nanoscale fundamentals, advances and prospects, *Light Sci. Appl.* **6**, e17039 (2017).
 - [3] C. Bradac, Nanoscale optical trapping: A review, *Adv. Opt. Mater.* **6**, 1800005 (2018).
 - [4] A.-I. Bunea and J. Glückstad, Strategies for optical trapping in biological samples Aiming at microrobotic surgeons, *Laser & Photonics Rev.* **13**, 1800227 (2019).
 - [5] Y. Yuan, C. Gu, S. Huang, L. Song, and F. Fang, Advances on studying optical forces: Optical manipulation, optical cooling and light induced dynamics, *J. Phys. D: Appl. Phys.* **53**, 283001 (2020).
 - [6] M. Xie, A. Shakoor, and C. Wu, Manipulation of biological cells using a robot-aided optical tweezers system, *Micromachines* **9**, 245 (2018).
 - [7] H. Zhang and K. K. Liu, Optical tweezers for single cells, *J. R. Soc. Interface* **5**, 671 (2008).
 - [8] R. A. B. Suarez, A. A. R. Neves, and M. R. R. Gesualdi, Optical trapping with non-diffracting airy beams array using a holographic optical tweezers, *Opt. Laser Technol.* **135**, 106678 (2021).
 - [9] H. Rubinsztein-Dunlop, A. Forbes, M. V. Berry, M. R. Dennis, D. L. Andrews, M. Mansuripur, C. Denz, C. Alpmann, P. Banzer, T. Bauer, E. Karimi, L. Marrucci, M. Padgett, M. Ritsch-Marte, N. M. Litchinitser, N. P. Bigelow, C. Rosales-Guzmán, A. Belmonte, J. P. Torres, T. W. Neely, M. Baker, R. Gordon, A. B. Stilgoe, J. Romero, A. G. White, R. Fickler, A. E. Willner, G. Xie, B. McMorrán, and A. M. Weiner, Roadmap on structured light, *J. Opt.* **19**, 013001 (2017).
 - [10] N. K. Efremidis and D. N. Christodoulides, Abruptly autofocusing waves, *Opt. Lett.* **35**, 4045 (2010).
 - [11] I. Chremmos, N. K. Efremidis, and D. N. Christodoulides, Pre-engineered abruptly autofocusing beams, *Opt. Lett.* **36**, 1890 (2011).
 - [12] P. Zhang, J. Prakash, Z. Zhang, M. S. Mills, N. K. Efremidis, D. N. Christodoulides, and Z. Chen, Trapping and guiding microparticles with morphing autofocusing Airy beams, *Opt. Lett.* **36**, 2883 (2011).
 - [13] I. Chremmos, P. Zhang, J. Prakash, N. K. Efremidis, D. N. Christodoulides, and Z. Chen, Fourier-space generation of abruptly autofocusing beams and optical bottle beams, *Opt. Lett.* **36**, 3675 (2011).
 - [14] D. G. Papazoglou, N. K. Efremidis, D. N. Christodoulides, and S. Tzortzakis, Observation of abruptly autofocusing waves, *Opt. Lett.* **36**, 1842 (2011).
 - [15] I. D. Chremmos, Z. Chen, D. N. Christodoulides, and N. K. Efremidis, Abruptly autofocusing and autodefocusing optical beams with arbitrary caustics, *Phys. Rev. A* **85**, 023828 (2012).
 - [16] S. Liu, M. R. Wang, P. Li, P. Zhang, and J. L. Zhao, Abrupt polarization transition of vector autofocusing Airy beams, *Opt. Lett.* **38**, 2416 (2013).
 - [17] F. Wang, C. L. Zhao, Y. Dong, Y. M. Dong, and Y. J. Cai, Generation and tight-focusing properties of cylindrical vector circular Airy beams, *Appl. Phys. B: Lasers Opt.* **117**, 905 (2014).
 - [18] B. Chen, C. D. Chen, X. Peng, Y. L. Peng, M. L. Zhou, and D. M. Deng, Propagation of sharply autofocused ring Airy Gaussian vortex beams, *Opt. Express* **23**, 19288 (2015).
 - [19] J. Zhao, Z. Zhang, Y. Liang, X. Sui, B. Liu, Z. Yan, Y. Zhang, and C. Changdong, Abruptly autofocusing beams generated with multiple Bessel-like beams, *J. Opt.* **18**, 035601 (2016).
 - [20] R.-S. Penciu, K. G. Makris, and N. K. Efremidis, Nonparaxial abruptly autofocusing beams, *Opt. Lett.* **41**, 1042 (2016).

- [21] Y. F. Jiang, K. K. Huang, and X. H. Lu, Radiation force of abruptly autofocusing Airy beams on a Rayleigh particle, *Opt. Express* **21**, 24413 (2013).
- [22] M. Chen, S. Huang, W. Shao, and X. Liu, Optical force and torque on a dielectric Rayleigh particle by a circular Airy vortex beam, *J. Quant. Spectrosc. Radiat. Transfer* **208**, 101 (2018).
- [23] W. Lu, X. Sun, H. Chen, S. Liu, and Z. Lin, Abruptly autofocusing property and optical manipulation of circular Airy beams, *Phys. Rev. A* **99**, 013817 (2019).
- [24] N. K. Efremidis, Z. Chen, M. Segev, and D. N. Christodoulides, Airy beams and accelerating waves: An overview of recent advances, *Optica* **6**, 686 (2019).
- [25] F. Lu, L. Tan, Z. Tan, H. Wu, and Y. Liang, Dynamical power flow and trapping-force properties of two-dimensional Airy-beam superpositions, *Phys. Rev. A* **104**, 023526 (2021).
- [26] M. V Berry and N. L. Balazs, Nonspreading wave packets, *Am. J. Phys.* **47**, 264 (1979).
- [27] Y. Kaganovsky and E. Heyman, Wave analysis of Airy beams, *Opt. Express* **18**, 8440 (2010).
- [28] Y. Liang, Y. Hu, Z. Ye, D. Song, C. Lou, X. Zhang, J. Xu, R. Morandotti, and Z. Chen, Dynamical deformed Airy beams with arbitrary angles between two wings, *J. Opt. Soc. Am. A* **31**, 1468 (2014).
- [29] Y. Liang, Y. Chen, and L. Wan, Propagation and power flow of high-order three-Airy beams, *Opt. Commun.* **405**, 120 (2017).
- [30] Y. Chen, X. Lin, S. Lin, S. Mo, L. Wan, and Y. Liang, Propagation dynamics of deformed 2D vortex Airy beams, *Chin. Opt. Lett.* **15**, 080801 (2017).
- [31] H. Wu, X. Zhang, P. Zhang, P. Jia, Z. Wang, Y. Hu, Z. Chen, and J. Xu, Optical pulling force arising from nonparaxial accelerating beams, *Phys. Rev. A* **103**, 053511 (2021).
- [32] Y. Liang, G. Liang, Y. Xiang, J. Lamstein, R. Gautam, A. Bezryadina, and Z. Chen, Manipulation and Assessment of Human Red Blood Cells with Tunable “Tug-of-War” Optical Tweezers, *Phys. Rev. Appl.* **12**, 064060 (2019).
- [33] J. Du, C. H. Yuen, X. Li, K. Ding, G. Du, Z. Lin, C. T. Chan, and J. Ng, Tailoring optical gradient force and optical scattering and absorption force, *Sci. Rep.* **7**, 18042 (2017).
- [34] Y. Jiang, J. Chen, J. Ng, and Z. Lin, Decomposition of optical force into conservative and nonconservative components, [arXiv:1604.05138](https://arxiv.org/abs/1604.05138) (2016).
- [35] X. Li, H. Zheng, C. H. Yuen, J. Du, J. Chen, Z. Lin, and J. Ng, Quantitative study of conservative gradient force and non-conservative scattering force exerted on a spherical particle in optical tweezers, *Opt. Express* **29**, 25377 (2021).
- [36] H. Zheng, X. Yu, W. Lu, J. Ng, and Z. Lin, GCforce: Decomposition of optical force into gradient and scattering parts, *Comput. Phys. Commun.* **237**, 188 (2019).
- [37] R. Gautam, Y. Xiang, J. Lamstein, Y. Liang, A. Bezryadina, G. Liang, T. Hansson, B. Wetzel, D. Preece, A. White *et al.*, Optical force-induced nonlinearity and self-guiding of light in human red blood cell suspensions, *Light Sci. Appl.* **8**, 31 (2019).